JACS
JOURNAL OF THE AMERICAN CHEMICAL SOCIETY

pubs.acs.org/JACS
Article

Ultrafast Formation of Aza-Quinone Methides from Suitably Substituted *o*-Hydroxymethylanilines Involves Higher Excited States

Yifan Su, Nađa Došlić,* Manuel Martinović, Mladena Glavaš, Josip Draženović, Jiani Ma,* and Nikola Basarić*

Cite This: *J. Am. Chem. Soc.* 2026, 148, 17662−17674
Read Online

ABSTRACT: Aza-quinone methides (aza-QMs) are important intermediates for the synthesis of aza-heterocycles, yet mild methods for their generation remain scarce. Here, we combine experimental and theoretical studies to guide the rational design of aza-QM precursors in efficient photoreactions. Photochemical elimination of H_2O from 2-aminobenzyl alcohol (**1**) serves as a promising starting point. We show that aza-QM formation from **1** is a relatively slow, multistep process involving heterolytic cleavage on the first singlet excited state (S_1), formation of a contact ion pair, relaxation to the ground state (S_0), and final deprotonation. In the newly designed *N*-Boc-*O*-Ac-aminobenzyl alcohol (**5**), the Boc group increases NH acidity and enforces a reactive conformation, while replacement of OH with an acetyl group introduces a low-energy nπ^* state. Benzylic C−O bond elongation stabilizes this state, promoting OAc elimination and enabling a highly efficient pathway. Aza-QM generation from **5** is an ultrafast, intermediate-free process that proceeds via conical intersections from **5** (S_1) to the aza-QM in S_0. Notably, in **5**, and possibly in **1**, the benzylic C−O bond cleavage ultimately occurs along their respective dissociative nσ^* states. We hope that these mechanistic insights will enable rational design of aza-QM precursors in multistep organic synthesis and in biological applications, where precise control of reactive intermediates is essential to avoid undesired interactions with biomolecular substrates.

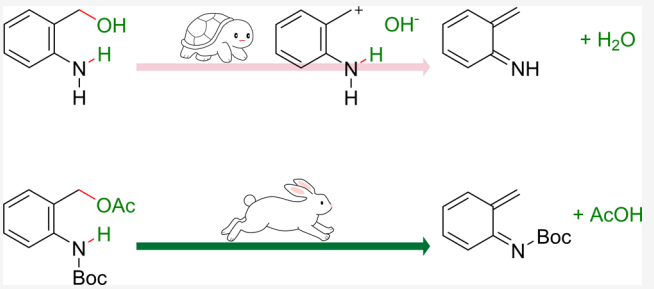

INTRODUCTION

Quinone methides (QMs) are commonly encountered reactive intermediates in the chemistry and photochemistry of phenols,[1,2] that have been revitalized in the last ten years for the various applications in organic synthesis.[3−5] Still dormant, but very useful intermediates are their aza-analogues, aza-quinone methides (aza-QM), which are excellent synthons for the preparation of aza-heterocycles.[6−8] For example, they have been employed in the [4 + 2] cycloadditions in the construction of dihydroquinolines,[9,10] formal [4 + 3] cycloadditions with nitrones,[11] [4 + 1] cycloadditions in the preparation of indoles,[12] or triarylmethanes and spiroindolines.[13] However, their chemistry has yet to flourish, which will be facilitated if new convenient methods for their preparation under mild conditions at room temperature are discovered.[14] Namely, the generation of aza-QMs in the ground state typically involves the breaking of aromaticity, for which harsh conditions are needed.[6−13]

Photochemical synthesis,[15] and particularly photocatalysis[16−18] has been in the focus of synthetic organic chemists in the past decade owing to numerous examples of complex molecular constructions, which were approached using photochemistry as the key step.[19,20] In that context, it is important to develop photochemical methodology to prepare aza-QMs, which would then be further used in organic synthesis, or biology. The photochemical methods are much milder compared to the thermal since they rely on the use of only photons (no reagents), at ambient temperature, which can be accomplished with spatial and temporal control. However, only a few photochemical strategies for generating aza-QMs have been reported to date. The most exploited is the approach by Kutetaladze et al., who developed an efficient protocol for the generation of aza-QMs based on the excited-state intramolecular proton transfer (ESIPT) from an amine to a carbonyl at the phenylene *ortho*-position.[21] The reaction has been used in the synthesis of complex heterocyclic systems.[22−26] An older and far less explored strategy is the photodehydration of *o*-hydroxymethylaniline (**1** in Chart 1), originally proposed by Yang and Wan.[27] The reactivity, stability, and aqueous acidity of **aza-QM·1** (Scheme 1) and its protonated form were studied a few years ago,[28] but the

Received: December 3, 2025
Revised: April 8, 2026
Accepted: April 14, 2026
Published: April 24, 2026

https://doi.org/10.1021/jacs.5c21621
J. Am. Chem. Soc. 2026, 148, 17662−17674

Chart 1. Investigated Aniline Derivatives 1−5 and 5a′ Undergoing Photoelimination to aza-QMs

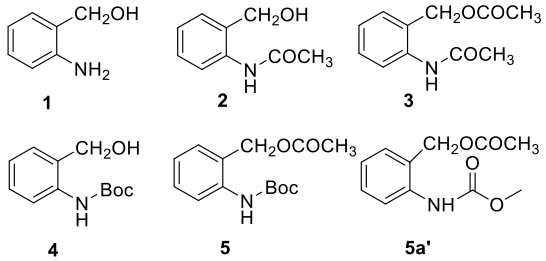

topic has not been explored further. A likely reason is the reactivity of **aza-QM·1** with the aniline precursor as a nucleophile, giving rise to oligomeric products. However, new reactions that can give rise to complex structures from simple precursors are needed, since these significantly increase the chemical space,[29] particularly needed in the context of medicinal chemistry.[30,31] Here, we show that the generation of aza-QM from **1** is amenable to systematic improvement.

Chemical substitution is a standard strategy for modulating photoreactivity.[32−34] Substituent effects can be broadly classified as inertial, steric, or electronic. Inertial effects arise from the mass of the substituent, which can slow nuclear motions such as torsional motion[35] or peptide bond pyramidalization.[36] Steric effects allow control over molecular conformation, with bulky groups restricting the system to more or less reactive geometries. Thus, the NEER effect (non equilibration of excited state rotamers) is a well-known effect in photochemistry affecting the reactivity.[37,38] Electronic effects, arising from the introduction of electron-donating or -withdrawing groups, can modify the topography of the relevant potential energy surfaces (PESs), as shown in adenine and 9-methyladenine,[39] as well as in and small organic systems including malonaldehyde, acetylacetone or hexafluoroacetylacetone.[40−43] However, none of these strategies alone is sufficient to control the photochemistry of **1**.

Here, we introduce chemical substituents in **1** that modify the intrinsic mechanism of the reaction by introducing new electronic states into play. This enables efficient aza-QM formation via elimination of small molecules (AcOH) from the aniline derivative **5** (Chart 1). Specifically, the Ac group introduces a low-lying nπ^* state localized on the −OAc moiety. Although this state lies above the initially excited $\pi\pi^*$ state, small geometric distortions can bring the nπ^* below the $\pi\pi^*$ state, providing an additional pathway for ultrafast formation of aza-QM. In addition to studying the parent molecule **1** and derivative **5**, we also examined how other nitrogen and oxygen substitutions affect the efficiency of the photoelimination reaction. The nitrogen atom was substituted with electron-withdrawing acetyl (Ac, in**2**, **3**) or *tert*-butoxycarbonyl (Boc, in **4**, **5**) groups to increase the NH acidity and influence molecular conformation, while the alcohol OH was converted into a better leaving group by substituting it with an Ac group (in **3**, **5**).

The photochemical reactivity was investigated by preparative irradiations in CH_3OH, where the formation of methanolysis products denote the photochemical pathways taking place via aza-QM intermediates. To get more insight into the processes taking place in the excited state and detect aza-QMs and other intermediates, steady-state and time-resolved fluorescence spectroscopy, and transient absorption spectroscopy (TAS) were conducted. Photochemical reaction mechanism for the generation of aza-QMs was proposed based on TAS measurements and computations, which corroborated experimental findings. We demonstrate that efficient ultrafast photoelimination takes place, albeit with different mechanisms. Aniline **1** delivers carbocation that subsequently deprotonates to aza-QM, while for **5**, aza-QM intermediate is directly formed in the ground state via easily accessible conical intersections (CI).[44−46] Beyond this broad picture, however, understanding the mechanistic details and detecting all intermediates en route to the aza-QMs is important for their practical application, particularly in biological systems.

RESULTS

Synthesis and Photochemistry

Preparation of **2**−**5** was based on a simple synthetic methodology for the introduction of Ac or Boc groups to the commercially available parent molecule **1** (see Schemes S1−S6 in the Supporting Information).

Photochemical reactivity of **1**−**5** was probed by irradiating CH_3OH solutions, where the formation of methanolysis products (**OCH_3·1**−**OCH_3·4**) indirectly indicated elimination reaction via aza-QM intermediates (**aza-QM·1**−**aza-QM·4**, Scheme 1).[27] The photomethanolysis reaction of **1** was not clean, as reported by Yang and Wan.[27] In addition to the anticipated product **OCH_3·1**, formation of numerous products took place (Figure S1 in the Supporting Information) due to nucleophilic attack of the amine in **1** to the aza-QM structure.[27] On the contrary, photolysis of **2** afforded mostly **OCH_3·2** (63%), but the irradiation over 46 h was required (Table S3 in the Supporting Information). Furthermore, photolyses of **3** and **4** gave the anticipated **OCH_3·2** (43%),

Scheme 1. Photomethanolysis of 1−5, and Quantum Yields for the Formation of Methanolysis Products OCH_3·1−OCH_3·4 From 1−5 upon Irradiation in CH_3OH Solutions (Φ_R)[a,b]

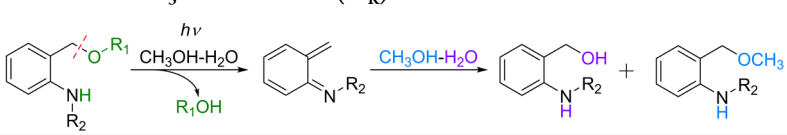

1, R_1=R_2=H	**aza-QM·1**, R_2=H	**1**	**OCH_3·1**, R_2=H	Φ_R[a]=0.40[b]
2, R_1=H, R_2=Ac **3**, R_1=R_2=Ac	**aza-QM·2**, R_2=Ac	**2**	**OCH_3·2**, R_2=Ac	Φ_R[a]=0.02 ± 0.03 Φ_R[a]=0.07±0.01
4, R_1=H, R_2=Boc **5**, R_1=Ac, R_2=Boc	**aza-QM·4**, R_2=Boc	**4**	**OCH_3·4**, R_2=Boc	Φ_R[a]=0.019±0.004 Φ_R[a]=0.49±0.06

[a]The irradiations were performed in CH_3OH solutions at 254 nm, and KI/KIO_3 as an actinometer was used (Φ_{254} = 0.74).[47,48] The composition of the irradiated solution was analyzed by HPLC. [b]Taken from ref 27.

https://doi.org/10.1021/jacs.5c21621
J. Am. Chem. Soc. 2026, 148, 17662−17674

Scheme 2. Irradiation of 5 in the Presence of Ethyl Vinyl Ether (EVE)

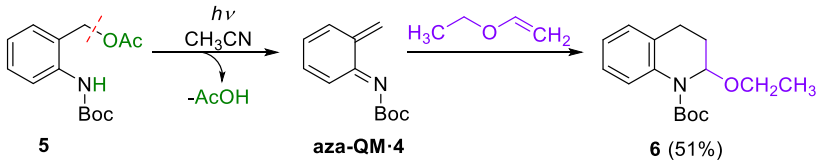

and OCH_3·4 (11%), and over long irradiations some side products were formed (Schemes S9 and S10 in the Supporting Information) in the competing cleavage reactions of the *N*-Ac, *N*-Boc or O-Ac groups. In contrast, the photomethanolysis of **5** was very clean and efficient. Irradiation of **5** in CH_3OH-H_2O (3:1 v/v, 4h, 300 nm) gave rise to the complete conversion and formation of two solvolysis photoproduct, OCH_3·**4** and **4**, which were isolated in 39% and 20% yield, respectively.

Quantum yield of the photomethanolysis reaction (Φ_R) was measured by the use of KI/KIO_3 as an actinometer (Φ_{254} = 0.74).[47,48] The Φ_R values for **1** (0.40) and **5** (0.49) are similar, whereas for **2**−**4** are significantly lower (Scheme 1). Note, however, that the methanolysis reaction of **5** is clean, contrary to the reaction of **1**.

Irradiation of **5** was also conducted in CH_3CN to which ethyl vinyl ether (EVE) was added, which is a known quencher of QMs, reacting with them in the Diels−Alder cycloadditions.[3,49−51] The irradiation gave rise to the tetrahydroquinoline cycloadduct **6**, isolated in 51% yield (Scheme 2). The isolation of **6** is a strong indication that aza-QM intermediate is formed in the photoelimination of acetic acid from **5**.

Photophysical Properties

The photophysical properties of **1**−**5** were investigated in CH_3CN solutions (for all data see Figures S6−S15 and Tables S4 and S5). The absorption spectrum of **1** is characterized by two low-energy absorption bands at ≈290 and ≈240 nm (Figure S6 and Table S4 in the Supporting Information), that based on the computations correspond to $\pi\pi^*$ transitions (vide infra). Compared to **1**, in the absorption spectra of **2**−**5** (Figures S7−S10), the lowest energy absorption bands are hypsochromically shifted (≈up to 10 nm), have lower oscillator strength and appear as shoulders, whereas the main absorption bands at ≈240 nm are not significantly affected. Thus, the energies of the S_1 states of **2**−**5** are positioned higher in energy by the introduction of the electron withdrawing Ac or Boc groups, and based on computation can be assigned to $\pi\pi^*$ transitions (vide infra). Note that Ac and Boc groups influence the nature and energy ordering of the low-lying excited states (S_2-S_4), as they introduce $n\pi^*$ and $\pi\pi^*$ states localized on the carbonyl groups of **2**−**5**.

Fluorescence spectra were measured in CH_3CN, and quantum yields of fluorescence were measured by use of *N*-acetyltryptophanamide in water as a reference (Φ_f = 0.12).[52] Fluorescence spectra of **1** and **4** in CH_3CN have maxima at 332 nm, and 303 nm, respectively. On the contrary, the spectra of **2**, **3** and **5** show the typical dual fluorescence with the main bands at 305−325 nm, and additional weaker bathochromically shifted bands at ≈450−490 nm. The later emission likely originates from minima of initially higher-lying excited states that, during the relaxation dynamics, descend below the initially excited $\pi\pi^*$ state (vide infra). Moreover, the Φ_f for **1** is significantly higher compared to the values for **2**−**5** (particularly for **2**, **3** and **5** which also show dual fluorescence) where the fluorescence is at the limits of the detection (Φ_f < 0.01, Table S4 in the Supporting Information). Thus, the introduction of the *N*- and/or *O*-substituents affected the emissive properties of the molecules by increasing the accessibility of nonradiative deactivation channels, and for **2**, **3**, and **5** by population of another weakly emissive species.

Fluorescence decays for **1**−**5** in CH_3CN were measured by time-correlated single photon counting (Figures S11−S15 and Table S5 in the Supporting Information). The decays could not be fit to single exponential functions; a sum of two or three exponents was used. The decay for **1** was fit to a sum of two exponents, with a small contribution of a very fast decay component (≈150 ps), which could not be estimated precisely on the setup used, and the major decay component of 2.6 ns. Such a dual fluorescence may originate from the two H-bonded conformers of **1** (vide infra). Similarly, in derivative **4**, two exponential decay of fluorescence may be attributed to different conformers that are emissive. On the other hand, for molecules **2**, **3**, and **5**, the fluorescence detected at 320 nm was fit to a sum of three exponents that have very short (≈100−150 ps) major decay component. The fast decay is related to the efficient nonradiative deactivation (and hence low Φ_f), and probably, to the population of species emitting at higher wavelengths.

Conformational Equilibria and Computed Spectra

Geometries and relative energies of the most stable conformers of **1**−**5** optimized with MP2/cc-pVDZ, together with their ADC(2)/cc-pVZD vertical excitation energies and dominant natural transition orbitals (NTOs) pairs contributing to the two lowest excited electronic states are given in Figures S16−S28 and Tables S6−S18 in the Supporting Information. Cartesian coordinates of all relevant structures are given in the Supporting Information Section 7.

We focus here on compounds **1** and **5**, since they undergo significantly more efficient H_2O or AcOH elimination reaction in the investigated series (Scheme 1). A comparison with compounds **2**−**4** is presented in the Discussion Section. In the electronic ground state, the lowest energy conformer of **1**, denoted **1a** features a O···H−NH hydrogen bond (see Figure S16 for the geometry and numeration of atoms), while the O−H···NH_2 conformer, denoted **1b**, is found 0.45 (0.42) kcal/mol higher in energy in the gas phase (CH_3CN) (Table S6). We note that a synchronous elimination of H_2O to generate aza-QM is possible only from conformer **1a** in which the amino group donates the proton to the hydroxyl group (d(N−H···O) ≈ 2.11 Å). However, the H_2O elimination does not necessarily proceed via a synchronous mechanism (vide infra), as previously reported in the literature.[28]

In the most stable conformer of **5**, denoted **5a**, the H-bond is formed between the amide group as a donor and the carbonyl oxygen atom of the Ac group (Figure S26 and Table S16). The distance between the proton of the amide group and the mentioned oxygen atom is 1.97 Å, which is 0.14 Å shorter that in **1a**, implying possibility of a more efficient synchronous

https://doi.org/10.1021/jacs.5c21621
J. Am. Chem. Soc. 2026, 148, 17662−17674

elimination of the AcOH. In conformer **5b**, the corresponding N−H···O distance increases to 2.09 Å, reducing the likelihood of synchronous AcOH elimination.

Vertical excitation energies of **1a** are listed in Table S7. The two lowest excited singlet states appear at 4.78 eV (S_1) and 5.83 eV (S_2). In CH_3CN, these states shift to 4.79 eV (S_1) and 5.78 eV (S_2), in good agreement with the experimental values. The two transitions arise from two linear combinations of $\pi\pi^*$ excitations delocalized on the phenyl ring. Figure S17 shows the dominant NTOs corresponding to these transitions. Apart from excitation on the phenyl ring, excitation to either S_1 or S_2 induces charge redistribution on the nitrogen and oxygen atoms. These states can therefore be regarded as precursors for the OH detachment (vide infra), since nuclear motion in these states is likely to elongate the C−O bond and potentially lead to the crossing with dissociative nσ^*states, which lie very high in energy at the Franck Condon (FC) geometry.[53,54]

The two lowest excited states of **5a** are found at 4.85 (4.86) eV and 5.60 (5.59) eV in the gas phase (CH_3CN) (Table S16). At the FC geometry, the third electronic state is only 0.28 eV above the second singlet. From the analysis of the dominant NTOs (Figure S27) one can see that S_1 and S_2 can be described as $\pi\pi^*$ states, while the S_3 state has nπ^* character with the excitation localized on the Ac group. Extension of the C−O bond (vide infra) stabilizes the S_3(nπ^*) state, which then becomes S_1(nπ^*). In **5b**, the nπ^* state at 5.79 eV is 0.89 and 0.20 eV above the two $\pi\pi^*$states at 4.90 and 5.59 eV. This explains the dual fluorescence in the steady-state spectrum, arising from the presence of both a $\pi\pi^*$ and an nπ^* minimum on the S_1 PES.

Nonadiabatic Dynamics for 1 and 5

To elucidate the mechanism of photoinduced C−O bond cleavage and assist in TAS assignment (vide infra), gas-phase surface-hopping nonadiabatic dynamics simulations (NAD) of compounds **1** and **5** were performed using the fewest-switches algorithm (see Computational Methods and Section 5 in the Supporting Information).[55] These gas-phase simulations aim to reveal plausible photochemical pathways and are not intended for direct quantitative comparison with experiments performed in pure or mixed solvents. The proposed mechanisms were validated and refined through molecular dynamics simulations in explicit water and reaction-path calculations in implicit solvent. NAD simulations were performed for the most stable conformer of **1**, **1a**, and model compound **5a′** in which the *tert*-butyl group of **5** was substituted with a methyl group (Figure 1). Since the *tert*-butyl group is not photochemically active in the excitation range of 270−282 nm, its substitution with a methyl group has a negligible effect on the photodynamics (compare the vertical excitation energies in Table S18 and the character of the lowest excited states in Figures S27 and S28), while it accelerates the calculations. SH trajectories were initiated from the S_1 state of **1a** and **5a′** and propagated for 1 ps in the manifold of three excited states (S_1−S_3) and the ground state (S_0). At the end of the simulation, 10% of **1a** trajectories (8/80) and 28% of **5a′** trajectories (20/78) reached the ground state, indicating faster relaxation and photochemistry for **5a′** (see Figure S30). For **1a**, the number of trajectories reaching the ground state is too low to draw conclusions about the dominant deactivation mechanism. Two illustrative SH trajectories showing photoelimination of H_2O via a S_1/S_0 CI and the cleavage of the C−O bond in the S_1 state leading to the formation of a contact ion pair (CIP) are analyzed in Figures S31 and S32. As noted, the majority of trajectories remained trapped in the S_1 state, consistent with its high fluorescence quantum yield of **1**.

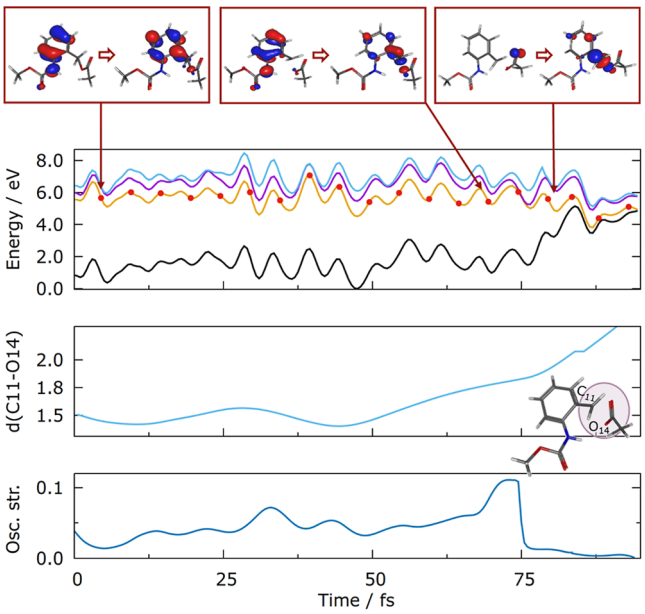

Figure 1. Top: time evolution of the potential energies of the three lowest singlet excited states (orange, purple, blue) and the ground state (black) of **5a′**. The red dots indicate the populated current state at a given time. The insets show the dominant NTO pairs describing the active electronic state at 10, 70, and 74 fs. Middle: time evolution of the C11−O14 bond. Bottom: the oscillator strengths of the S_1 state. The CI between the initially populated $S_1(\pi\pi^*)$ state and the S_1(nσ^*) states is encountered at ≈75 fs.

The relaxation of **5a′** is faster (Figure S30). The excited-state lifetime of **5a′** was determined by fitting its population decay to a monoexponential function, yielding the excited-state lifetime of $\tau \approx 3100$ fs. The dominant relaxation mechanism is the cleavage of the benzylic C−O bond (Figure 1). However, analysis shows that **5a′** undergoes fragmentation through two distinct mechanisms. The first mechanism, similar to the one found in **1**, is illustrated in Figure 1. The top panel displays the potential energy evolution of the three lowest singlet excited states and the ground state. The active state, that is the state populated during the dynamics is indicated by red dots. The trajectory evolves in the adiabatic S_1 state and at 95 fs reaches the S_1/S_0 CI through the C11−O14 bond cleavage (middle panel). This is accompanied by the decrease of the N15−H16···O14 distance from 2.29 Å at the start of the dynamics to 1.88 Å at the S_1/S_0 CI. In our simulation, the leaving fragment is $^{\bullet}$OAc not AcOH. The H-transfer likely occurs either in the CI region or after reaching the ground state; however, since ADC(2) is a single-reference method, the system's evolution near or beyond the S_1/S_0 CI cannot be reliably tracked. In the insets we show the dominant NTO pairs of the current state. Up to 75 fs, the trajectory stays in the $\pi\pi^*$state, after which it encounters a CI with an nσ^* state and switches to that state. Once in the nσ^* state, the S_1/S_0 CI is reached in less than 20 fs. The state's character change is also evident from the sharp change in the S_1 state oscillator strength, shown in the bottom panel of Figure 1.

Figure 2 shows a slower trajectory of **5a′** that reaches the S_1/S_0 CI at ≈750 fs (top), also by C11−O14 bond cleavage (middle). The main difference from the previous case is the

https://doi.org/10.1021/jacs.5c21621
J. Am. Chem. Soc. 2026, 148, 17662−17674

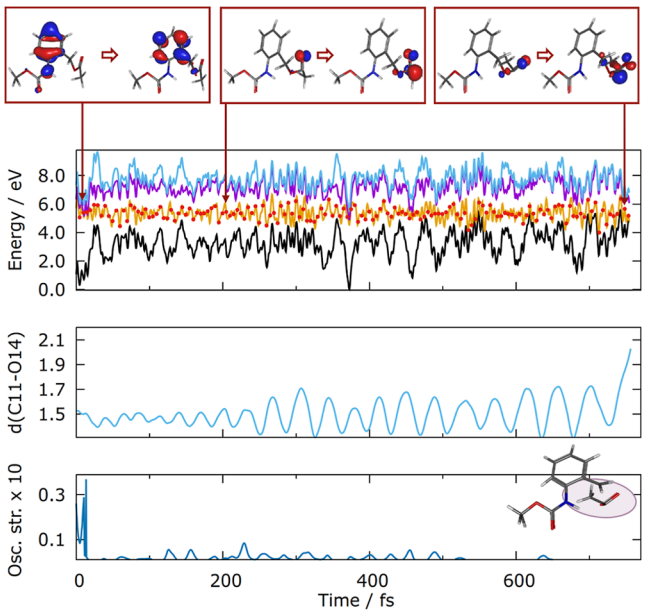

Figure 2. Top: time evolution of the potential energies of the three lowest singlet excited states (orange, purple, blue) and the ground state (black) of **5a′**. The red dots indicate the populated current state at a given time. Middle: time evolution of the C11−O14 bond. Bottom: the oscillator strengths of the S_1 state. The CI between the initially populated $\pi\pi^*$ state and the dark $n\pi^*$ state is encountered at ≈20 fs. At 740 fs a CI with the $n\sigma^*$ state is reached. The insets and Figure S33 show the dominant NTO pairs of the S_1 state at t = 0, 150, and 740 fs.

rapid loss of the oscillator strength (bottom) around 20 fs, caused by a nonadiabatic transition from the initially excited $\pi\pi^*$ state to the $n\pi^*$ state (S_3 at the FC geometry, Tables S17 ad S18) with the excitation localized on the OAc group (middle inset). This change in the S_1 state character is accompanied by an increase in the ground state potential energy by ≈3 eV (black curve). However, the system does not reach the CI with S_0 in the S_1 ($n\pi^*$) state because the C11−O14 bond is not stretched enough. Around 740 fs, a CI with the $n\sigma^*$ state is encountered (see Figure S33). This leads to a sudden extension of the C11−O14 bond and the CI with the ground state.

Reaction Paths for the Formation of aza-QM from 1 and 5

The reaction mechanisms suggested by NAD simulations can be better understood in a static framework. In the gas phase, NAD simulations indicate that both **1a** and **5a′** undergo homolytic cleavage of the benzylic C−O bond, although with different efficiencies. This process involves significant geometric rearrangement and, according to the simulations, may proceed through more than one electronic state. These results, however, require careful consideration, as solvent effects can substantially alter the reaction by modifying the relevant PESs. Furthermore, experiments were carried out in CH_3CN, but trace amounts of water cannot be excluded. Since water can form intermolecular hydrogen bonds with **1a** and **5a** and directly influence their photochemical reactions, molecular dynamics simulations in explicit water were performed. The results (Figure S29 in the Supporting Information) show that the two compounds experience different solvation environments. For **1a**, hydrogen bonds form between the amino nitrogen and water (N16···O ≈ 2.8 Å) and between the hydroxyl oxygen and water (O14···O ≈ 2.7 Å), motivating the inclusion of an explicitly hydrogen-bonded water molecule in the reaction-path calculations, which bridges the amino and hydroxyl groups. In contrast, **5a** is stabilized by an intramolecular hydrogen bond, which largely prevents the formation of a persistent intermolecular hydrogen bond with water.

Figures 3 and S34 show the reaction paths for the C−O bond cleavage in **1a·H₂O** and **1a**, respectively, optimized in

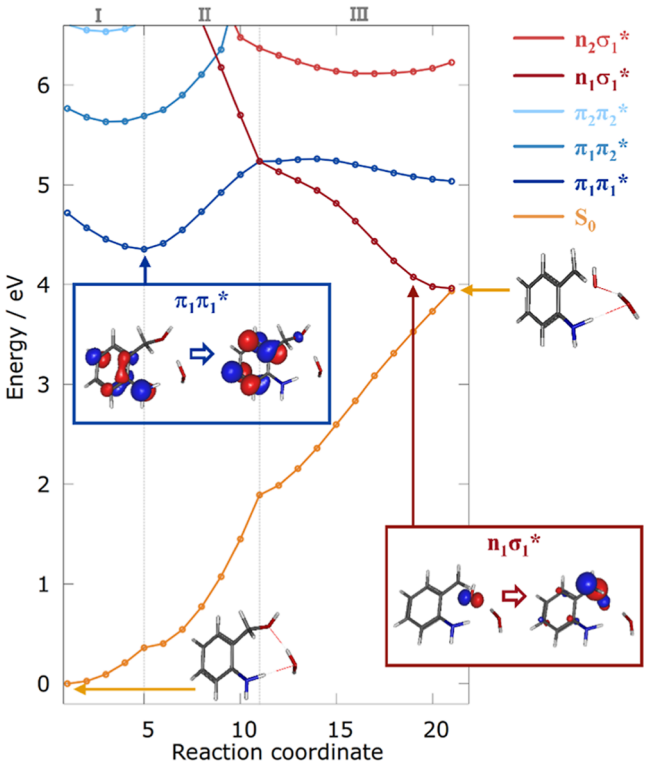

Figure 3. Potential energy profiles for C−O bond cleavage **1a·H₂O** in CH_3CN. The reaction paths are divided in three segments: from the FC geometry (the computed point 1 from left to right) to the $S_1(\pi\pi^*)$ minimum (point 5 from left to right), then to the $\pi\pi^*/n\sigma^*$ minimum energy CI (point 11), and then to the $S_1(n\sigma^*)/S_0$ CI (point 22). Three locally excited $\pi\pi^*$states (blue) and two dissociative $n\sigma^*$ states (red) are shown, together with the ground state (orange). Vertical excitation energies were computed at each geometry using ADC(2)/cc-pVDZ. Insets show the dominant NTO pairs of the lowest $\pi\pi^*$ state and the dissociative $n\sigma^*$ state, along with the molecular geometry at the S_1/S_0 CI. For comparison with **1a** see Figure S34 and for gas-phase reaction paths see Figures S35−S37 in the Supporting Information.

CH_3CN using the COSMO model. For comparison with reaction paths optimized in the gas phase see Figures S35−S37 in the Supporting Information. At first glance, the reaction paths for **1a·H₂O** and **1a**—starting from the respective FC geometries (dark blue line), passing through the minimum of the $\pi\pi^*$ state, and involving a barrier of ~0.4 eV relative to the FC geometries to reach the $S_2(n\sigma^*)/S_1(\pi\pi^*)$ CI, followed by the $S_1(n\sigma^*)/S_0$ CI at 4.43 eV (**1a**) and 3.96 eV (**1a·H₂O**)—appear qualitatively similar. They indicate that only a negligible fraction of **1a** or **1a·H₂O** can overcome this barrier, even when the ground-state zero-point energy contribution (≈0.2 eV) is taken into account. However, the main difference between the reaction profiles occurs after the $S_2(n\sigma^*)/S_1(\pi\pi^*)$ CI, where they diverge significantly. In both systems, the nonadiabatic

https://doi.org/10.1021/jacs.5c21621
J. Am. Chem. Soc. 2026, 148, 17662−17674

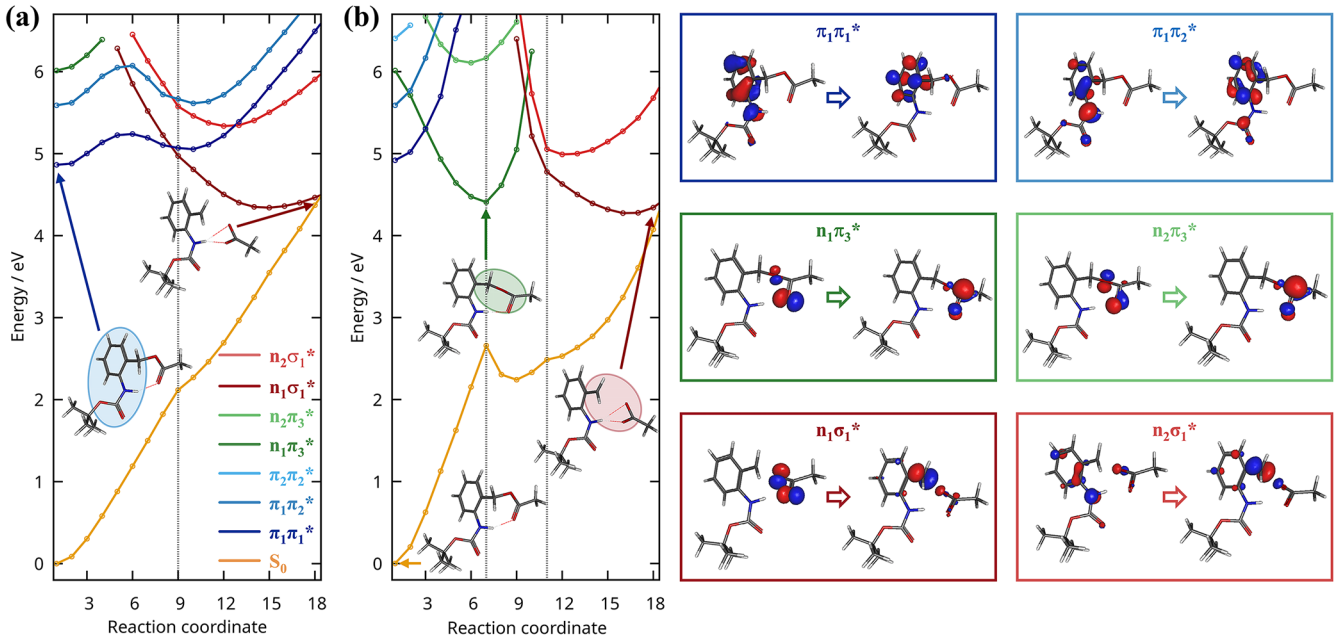

Figure 4. Potential energy profiles for C−O bond cleavage in **5a** in CH_3CN. Reaction paths: (a) from the FC geometry (point 1) to the $\pi\pi^*/n\sigma^*$ CI (point 9) and then to the S_1/S_0 CI, and (b) from the FC geometry (point 1) to the $n\pi^*$ minimum (point 7) and then to the S_1/S_0 CI (point18) via the $S_2(n\sigma^*)/S_1(n\pi^*)$ CI. Two $\pi\pi^*$ states (blue), two $n\pi^*$ states (green), and two dissociative $n\sigma^*$ states (red) are shown together with the ground state (orange). Vertical excitation energies were computed at each geometry using ADC(2)/cc-pVDZ in implicit solvent. Insets show the dominant NTOs pairs of the key electronic transitions. Geometries at the FC, $\pi\pi^*/n\pi^*$ CI, and S_1/S_0 CI are depicted, and the chromophores on which the excitations are localized are highlighted.

population transfer between the $\pi\pi^*$ and $n\sigma^*$ states may be inefficient but in **1a·H$_2$O** the extended plateau of the $\pi\pi^*$ state indicates that a radical pair—likely a CIP under experimental conditions—can form. This implies that the signature of **CIP-1** and carbocation intermediates (**cat-1**) may be detected by TAS. Overall, based on the present calculations, rapid C−O bond dissociation in **1** appears unlikely.

Based on the NAD simulations, two reaction profiles were constructed for C11−O14 bond dissociation in **5a** (Figure 4). The pathway shown in Figure 4a shares similarities with those of **1a** and **1a·H$_2$O**, as it involves a barrier (0.37 eV in **5a**) leading to the $S_2(n\sigma^*)/S_1(\pi\pi^*)$ CI. However, the key difference between **1a** and **5a** lies in the shape of the $\pi\pi^*$ state after this intersection. In **5a**, the $\pi\pi^*$ surface rises steeply after the $S_2(n\sigma^*)/S_1(\pi\pi^*)$ CI. This increases the probability of nonadiabatic population transfer to the dissociative $n\sigma^*$ state and it is expected to promote faster and potentially more efficient fragmentation of **5a**.

The reaction profile shown in Figure 4b features first a low-barrier transition from the initially populated $\pi\pi^*$ state (denoted $\pi_1\pi_1^*$, dark blue) to a $n\pi^*$ state, denoted $n_1\pi_3^*$, (S_3 at the FC geometry, green). Upon reaching the minimum of the $n_1\pi_3^*$ state, a slight elongation of the C11−O14 bond leads to a peaked CI with the dissociative $n_1\sigma^*$ state. Relative to the FC geometry, the barrier to the $n_1\pi_3^*/n_1\sigma^*$ CI is 0.43 eV, slightly higher than for the first pathway. However, the narrow barrier and peaked topography of this CI suggests that nonadiabatic transitions from the $n_1\pi_3^*$/to the $n_1\sigma^*$ state are more probable, leading to more efficient fragmentation.

Based on the reaction profiles shown in Figures 3 and 4, which connect selected minima and CI points, it is natural to question the robustness of the proposed mechanisms. However, the optimized reaction paths presented in Figures S39−S41 in the Supporting Information demonstrate that the reactions do not require passage through minimum-energy CI points. Instead, they proceed through extended regions of avoided crossing, where two electronic states, separated by up to ∼1 eV, interact strongly and gradually exchange electronic character. The presence of this extended $\pi\pi^*/n\sigma^*$ avoided-crossing region makes the mechanism significantly more robust than suggested by Figures 3 and 4 alone.

Femtosecond and Nanosecond TA Measurements

The TAS was used to probe for the formation of aza-QMs and other reactive intermediates. Laser flash photolysis (LFP) measurements were conducted in the Ar- or O_2-purged solutions, where the difference was anticipated due to the known quenching of triplets and radicals by O_2 (but not aza-QMs). Moreover, the measurements were conducted in CH_3CN and CH_3CN−PBS (4:1 v/v), where the addition of protic solvent was expected to affect the proton transfer pathways, which may be involved in the elimination of H_2O or AcOH. In the aqueous solvent the spectra and decay kinetics were measured also at different pH (in the presence of 50 mM phosphate or PBS buffer). It was reported that aza-QM from **1** was formed in a two-step process, that involved elimination of OH^-, followed by the deprotonation of aza-QM from the carbocation (the reported pK_a of the aza-QM is 10.6).[28] To assign the transients, the experimental data was compared to simulated spectra. For **1** and **5**, the ADC(2)/cc-pVDZ electronic absorption spectra (Figures S44 and S45) show good agreement with the experimental UV−vis spectra, with deviations from experiment of 25 and 3 nm, respectively. Based on the comparison between experimental and computational results for **1** and **5** (Tables S7, S17, S18 and Figures S44 and S45 in the Supporting Information), the most of femtosecond transient absorption (fs-TA) experiments used a 266 nm pump source, which excites the molecules to the S_1 state. In addition,

https://doi.org/10.1021/jacs.5c21621
J. Am. Chem. Soc. 2026, 148, 17662−17674

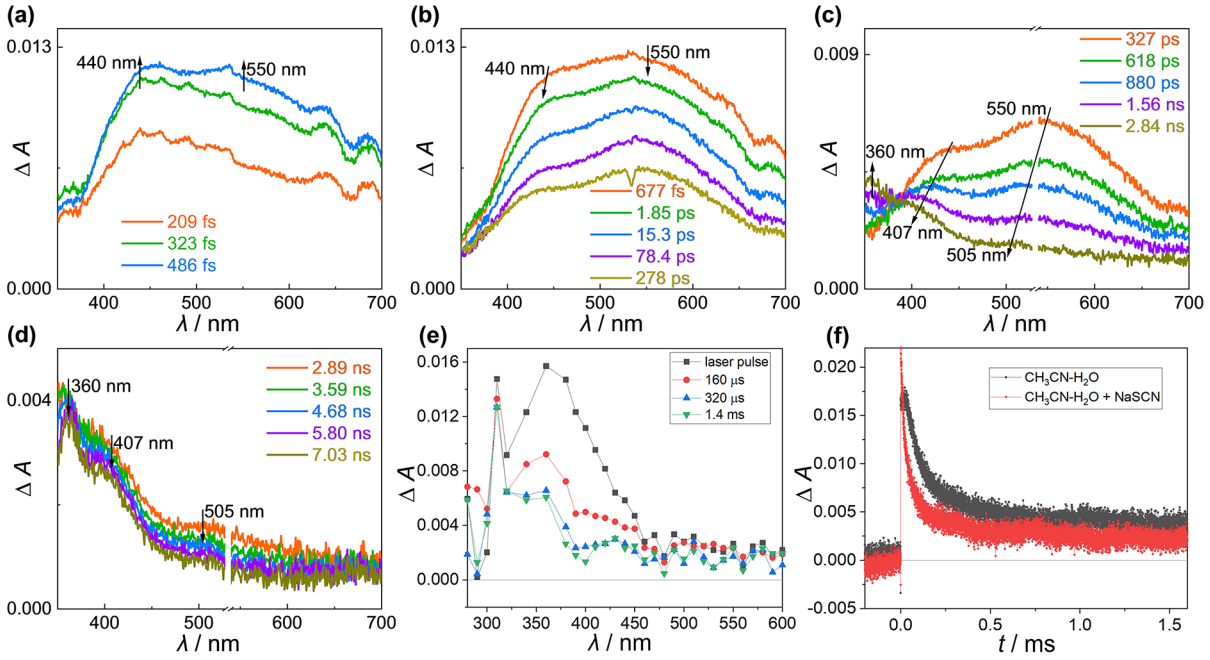

Figure 5. (a–d) fs-TA spectra of **1** in CH_3CN–PBS (4:1, v/v, pH = 7.4) (λ_{ex} = 266 nm). (e) TAS of **1** (λ_{ex} = 266 nm, A_{266} = 0.30, $c = 5.48 \times 10^{-4}$ M) in O_2-purged CH_3CN–H_2O (4:1, pH = 7.0, 50 mM sodium phosphate buffer). (f) Decay of TA at 390 nm for the solution of **1** without, and in the presence of NaSCN (0.11 M).

some measurements were conducted with the excitation at 245 and 300 nm.

By use of the laser irradiation at 266 nm, **1** in CH_3CN is excited to the FC geometry of the S_1 state (Figure S46) showing computed absorption at ≈370 nm and 550–700 nm (Figure S47). After that, it transfers very fast to IM1 with the typical signal at 440 and 550 nm. The fs-TA in CH_3CN–PBS solution (Figure 5a–d) is almost the same with that seen in pure CH_3CN, while the transformation from the FC S_1 to IM1 is faster in protic solvent. In aprotic solvent, the characteristic signal of IM1 is observed within 77 ps, while in a protic solvent, it is within 677 fs. The peak positions of IM1 in CH_3CN–PBS solution is the same with that in CH_3CN, while the intensity is different (Figures 5a–d and S46). Based on the NAD simulations (Figure S32) computed reaction energy profile (Figure 3) and computed TA spectra (Figures S48 and S53 in the Supporting Information), the IM1 was assigned to the singlet excited state CIP (denoted as **CIP-1** (S_1)) formed by heterolytic cleavage of the OH^- in the excited state. Subsequently, the signal of **CIP-1** (S_1) transformed to a new species IM2 absorbing at around 407 nm, as well as to IM3 and other species absorbing at 360 and 505 nm. It is suggested that the **CIP-1** (S_1) deactivates to **CIP-1** (S_0) through a slight torsion of the NH_2 group. Our computations (Figure S49) predict that **CIP-1** (S_0) absorbs between 350 and 400 nm, depending on the distance between the two ions. We therefore assign IM2 detected at 407 nm to **CIP-1** (S_0). In the ground state **CIP-1** (S_0) dissociates to give **cat-1** (S_0), which shows a computed absorption around 440 nm (Figure S50). This species subsequently deprotonates on a longer time scale to form **aza-QM·1** (S_0) absorbing at 360 nm (Figure S51) corresponding to the species detected on the millisecond time scale.[28] Recall also that **1** is fluorescent with the lifetime in nanoseconds (Table S5). The TA spectrum of **1a** computed at the $S_1(\pi\pi^*)$ minimum displays two intense transitions at 360 and 505 nm (Figure S52). Therefore, contributions from multiple species to the TA spectra on the nanosecond time scale should be taken into account. Consequently, the most persistent transient species detected by fs-TA on nanosecond time scale were assigned to **CIP-1** (S_0) absorbing at 407 nm, **aza-QM·1** (S_0) with the absorption at 360 nm, and relaxed **1a** (S_1) at 360 and 505 nm (for the comparison of all computed spectra of intermediates with the experimental spectra see Figures S47–S54 in the Supporting Information). The fs-TA data for **1** in CH_3CN–PBS solution was also fit globally. However, due to overlapping of the spectral features of too many species, a reliable model that could fit data could not be obtained (Figures S55 and S56 in the Supporting Information).

The computed PES for the photoelimination from **1** (Figure 3) indicates an energy barrier (vide supra). Consequently, it is plausible that excitation at different wavelengths may give rise to different observed rate constants for the formation of **CIP-1** (S_1) and subsequent transients. Therefore, we conducted fs-TA measurements for **1** in CH_3CN–PBS solution at different excitation wavelengths, 245 and 300 nm (Figures S57 and S58 in the Supporting Information). The spectra look qualitatively similar. However, no signal corresponding to the FC geometry of **1** was observed under 245 nm excitation, indicating that it rapidly formed **CIP-1** (S_1). On the contrary, a slower conversion of the FC of **1** to the **CIP-1** (S_1) under 300 nm excitation (within 500–600 fs) was observed. However, no significant difference was observed in the kinetics for the formation of **CIP-1** (S_0) and other transients under different excitation wavelengths.

In the ns-TA spectra of **1** in Ar-purged CH_3CN (Figure S60 in the Supporting Information), two transients were detected that absorbed at 300–450 nm and decayed with lifetimes $\tau \approx 1.4 \pm 0.2$ μs and $\tau \approx 19 \pm 1$ ms, and were not quenched by O_2, precluding their assignment to the triplet excited state of the molecule or radicals. The short-lived transient with the absorption at $\lambda > 400$ nm was tentatively assigned to the

https://doi.org/10.1021/jacs.5c21621
J. Am. Chem. Soc. 2026, 148, 17662–17674

solvated **cat-1** (S_0), whereas the long-lived transient with the absorption band at 360 nm was tentatively assigned to **aza-QM·1**. Attempts to quench the transient by EVE failed, and other quenching studies that would prove the assignment were not possible due to the very low intensity of the transient absorption. Note that we did not observe the transformation of one species to another with the decay of the fist matching the rise kinetics of the second, as reported by Sung et al.[28] The decay of TA was fit to a sum of two exponents not indicating that one transient was formed from the other.

In the aqueous solution of **1** at pH 4 (Figure S62 in the Supporting Information), two transients were detected in both Ar- and O_2-purged solution, that decayed with the lifetime of $\tau \approx 4.8 \pm 0.3$ μs and $\tau > 100$ μs, and their intensity was weak to allow further studies. On the contrary, at pH 7, the TA signal was stronger. Two transients were detected (Figures 5e and S64 in the Supporting Information); the short-lived one absorbed with the maximum at ≈ 400 nm and decayed with the lifetime of $\tau \approx 71 \pm 1$ μs. The longer-lived transient absorbed with the maximum at 360 nm, decayed with $\tau \approx 300 \pm 30$ μs. The purging by O_2 did not affect the intensity or the decay kinetics of the transients, suggesting that triplet excited states or radicals were not involved. To assign the transients detected at pH 7, quenching experiments were performed with nucleophiles NaN_3, and NaSCN (Figures S65−S69 in the Supporting Information), the ubiquitous quenchers of species such as cations,[56] aza-QMs or QMs.[28,49,49,50] Both nucleophiles quenched the faster decay component (for the rate constants see Table 1), which was assigned to **cat-1** (S_0).[56]

Table 1. Rate Constants (k_q) for the Quenching of Transients Determined by Ns-TA

compound	conditions	quencher	k_q/M^{-1} s^{-1}
1	CH_3CN-H_2O (4:1), pH 7	NaN_3	$(1.3 \pm 0.1) \times 10^8$
1	CH_3CN-H_2O (4:1), pH 7	NaSCN	$(1.0 \pm 0.2) \times 10^5$
5	CH_3CN	EVE	33 ± 1
5	CH_3CN	ethanolamine	$(5.8 \pm 0.2) \times 10^4$
5	CH_3CN-H_2O (4:1), pH 7	NaN_3	$(3.48 \pm 0.06) \times 10^5$
5	CH_3CN-H_2O (4:1), pH 7	NaSCN	$(1.00 \pm 0.03) \times 10^5$

The longer-lived decay component was also quenched by NaN_3, NaSCN and EVE (Figures S65−S69 in the Supporting Information), but we could not estimate precisely and accurately reliable rate constants. Consequently, we assign the transient with the lifetime of $\tau \approx 71 \pm 1$ μs to the carbocation **cat-1** (S_0), or protonated aza-QM, and the long-lived transient ($\tau \approx 300 \pm 30$ μs) is **aza-QM·1** (S_0).

The fs-TA spectra for **5** in $CH_3CN-PBS$ solution (Figure 6) are identical to those seen in pure CH_3CN (Figure S70). Upon excitation at 266 nm, a signal appears at 346 and 460 nm (Figure 6a), which is assigned to **5** (S_1). This signal stops rising after 727 fs, consistent with the nonadiabatic simulations for the model compound **5a′**. Subsequently, a signal emerges at 400 nm (Figure 6b), that is assigned to **aza-QM·4** (S_0) based on computed spectra (Figures S72 and S74 in the Supporting Information). The formation of **aza-QM·4** (S_0) likely occurs before 1.57 ps, but the signal is initially obscured by the stronger absorption of **5** (S_1). The global fitting of the fs-TA data for **5** indicated only two species (for the decay associated spectra see Figure S75 in the Supporting Information). The shorter time constant was assigned to the lifetime of **5** (S_1), and the long-lived species to **aza-QM·4** (S_0). Thus, upon excitation, the S_1 state of **5** was generated, followed by synchronous elimination of acetic acid to generate **aza-QM·4** (S_0), most probably via a CI, since other intermediates en route were not observed.

fs-TA spectra for **5** in $CH_3CN-PBS$ (4:1, v/v) were also measured upon excitation at 245 and 300 nm (Figures S76 and S77 in the Supporting Information). Qualitatively, they look similar as those upon excitation at 266 nm. However, the dynamics is different. Upon excitation at 245 and 266 nm the signal at 400 nm assigned to **aza-QM·4** (S_0) appears early (≈ 1 ps). However, the signals were different under 300 nm excitation. During the early stage of fs-TA, signals at 346, 425, and 460 nm appeared simultaneously. Based on the computation (Figure S73 in the Supporting Information), the signal at 425 nm was assigned to the relaxed **5** (S_1) n,π^* state. Subsequently, the signal at 346 nm decayed faster than the signal at 425 nm and the generation of **aza-QM·4** (S_0) was first observed at 18.8 ps. Thus, the fs-TA measurements are in line with the computations. Excitation at longer wavelength gives **aza-QM·4** (S_0) less efficiently in the slower process.

In contrast to the ns-TA spectra of **1**, only one transient species was detected by ns-TA from **5**, formed within the laser pulse, absorbing with the maximum at ≈ 400 nm (Figures 6c and S79−S88 in the Supporting Information). The transient decayed with the lifetime of $\tau \approx 0.5 \pm 0.2$ s in CH_3CN solution, and was not quenched by O_2 (Figures S80 and S83). The transient had somewhat slower decay kinetics in the aqueous solution, where it decayed with the lifetime $\tau \approx 0.21 \pm 0.02$ s (Figure S84 in the Supporting Information), and was also not quenched by O_2. Based on the insensitivity to O_2, position of the maximum in the spectra, and comparison to the computed spectra (Figures S72 and S74 in the Supporting Information) the transient was assigned to **aza-QM·4** (S_0). To verify the assignments, the quenching studies were performed with NaN_3, NaSCN and ethanolamine, as well as with EVE.[49−51] The values of all rate constants (Table 1) are in accord with the assignment of the transient to **aza-QM·4**. In particular, the quenching by EVE (Figure 6d), undoubtedly proved the assignment. Namely, other plausible electrophilic species such as carbocations may also be formed, and react with nucleophiles. However, the reactions of carbocations with nucleophiles proceed faster and the Diels−Alder reactions are not possible. Consequently, fs-TA and ns-TA experiments for **5** clearly gave rise to **aza-QM·4**, which was formed efficiently from **5** (S_1).

DISCUSSION

Based on the experimental and computational results, a mechanism for the H_2O elimination from the parent molecule **1** and AcOH elimination from derivative **5** can be proposed. The overall mechanism for the H_2O elimination from **1** to **aza-QM·1** (S_0) is shown in Scheme 3. After the initial population of **1** (S_1), it undergoes the cleavage of the C−O bond at the benzylic position. For this to occur, a crossing to an nσ^* state—where the σ^* orbital is localized on the bond to be cleaved—may be required, as indicated by the computed PES connecting the FC region to the S_1/S_0 CI. This result is noteworthy in the context of reactions that generate QMs or aza-QMs. Furthermore, NAD simulations and reaction-path scans in solution indicate that both OH· radical and H_2O

https://doi.org/10.1021/jacs.5c21621
J. Am. Chem. Soc. 2026, 148, 17662−17674

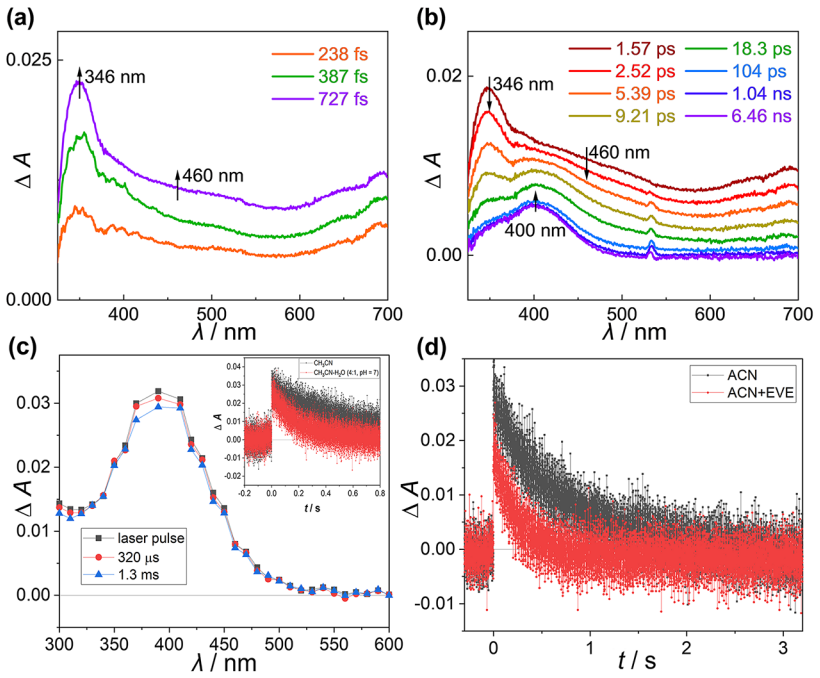

Figure 6. (a,b) fs-TA spectra of **5** in CH_3CN–PBS (4:1, v/v) (λ_{ex} = 266 nm). (c) TA spectra of **5** (λ_{ex} = 266 nm, A_{266} = 0.30, $c = 4.00 \times 10^{-4}$ M) in O_2-purged CH_3CN–H_2O (4:1, pH = 7.0, 50 mM sodium phosphate buffer). Inset: Decays at 390 nm for the O_2-purged solutions of **5** ($c = 4.00 \times 10^{-4}$ M) in CH_3CN and CH_3CN–H_2O (4:1) at pH 7. (d) Decay of the TA at 400 nm for the solution of **5** in CH_3CN, without and in the presence of EVE ($c = 4.00 \times 10^{-4}$ M).

Scheme 3. H_2O Photoelimination Mechanism from 1

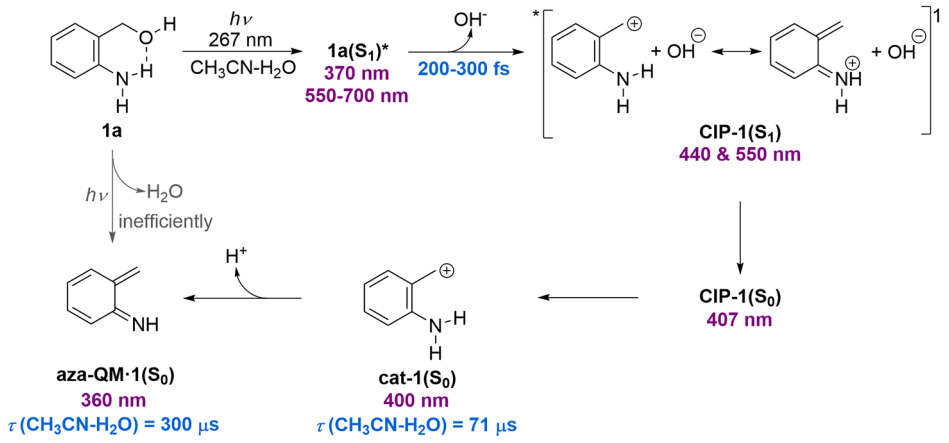

elimination are inefficient due to a broad energy barrier along the pathway from the **1** (S_1) FC to the nσ^* CI. Thus, **1** is characterized by high value of Φ_f, which is also the consequence of the presence of two conformers (**1a** and **1b**), where only **1a** is reactive, and **1b** is emissive.

The cleavage of the C–O bond in solution is most likely heterolytic, as indicated by the fs-TA experiments. The discrepancy between experiment and theory likely reflects current methodological limitations,[57] as current computational approaches cannot reliably describe heterolytic bond dissociation either in the gas phase or within implicit solvent models. Fragment-based quantum chemical methods capable of distinguishing between homolytic and heterolytic pathways are only now emerging and have so far been primarily applied to ground-state reactions in the gas phase.[58]

Notwithstanding these limitations, our computations for **1a·H_2O**, conducted in implicit CH_3CN and including an explicitly hydrogen-bonded water molecule bridging the NH_2 and OH groups (Figure 3), are generally in accord with the fs-TA experiments. Compared to gas-phase studies, we found that solvation strongly alters the topography of the PESs near the $S_2(n\sigma^*)/S_1(\pi\pi^*)$ CI, making excited-state OH^- elimination and formation of **CIP-1** (S_1) more favorable, in agreement with the fs-TA observations, which detect the formation of the first intermediate (IM1). Thereafter, the **CIP-1** (S_0) is generated via an easily accessible CI. Subsequently, **CIP-1** (S_0) undergoes dissociation to form free solvated carbocation **cat-1** (S_0), which was observed by TAS on the nano- and microsecond time scale. The N–H bond cleavage to form **aza-QM·1** (S_0) takes place over relatively a long time of 71 μs due to its strong basicity.[28] We also note a possibility for the direct formation of **aza-QM·1** (S_0) from **1** (S_1) based on computed PES and NAD, which is however inefficient minor pathway. Due to the direct formation of **aza-QM·1** (S_0) from **1** (S_1) the

https://doi.org/10.1021/jacs.5c21621
J. Am. Chem. Soc. 2026, 148, 17662–17674

rise kinetics of **aza-QM·1** (S_0) during the decay of **cat-1** (S_0) was not detected.

The computations for **5a** conducted for the gas phase and in implicit CH_3CN solution give rise to the same conclusions, which are in accordance with experiments. In the photochemistry of **5**, the substitution of nitrogen and oxygen by Boc and As group is beneficial. The steric bulk of the Boc forces the molecule to adopt the reactive conformation for the synchronous elimination of AcOH. Moreover, the Ac group brings in the dark nπ^* state, locally excited on the Ac. Although higher in energy then the lowest $\pi\pi^*$ state in the FC region, upon elongation of the C−O bond the energy of the nπ^* state is lowered and becomes S_1. Therefore, two ultrafast relaxation pathways are available to **5**. The first mechanism, similar to that operating in **1**, involves a direct crossing between the initially excited $\pi\pi^*$ state and the dissociative nσ^* state (Figure 4a). The second mechanism proceeds via internal conversion from the $\pi\pi^*$ to the localized nπ^*state, which was detected by fluorescence and fs-TA, followed by crossing with the nσ^* state (Figure 4b). In both cases, the elimination of AcOH requires the involvement of an nσ^* state. Therefore, **5** exhibits dual fluorescence with the emission from the $\pi\pi^*$ and nπ^* states. Once the nσ^* is reached, the cleavage of the C−O bond takes place delivering the **aza-QM·4** via the S_1/S_0 CI. In any case, both pathways directly populate **aza-QM·4** (S_0), which was shown experimentally by fs-TA (Scheme 4). We

Scheme 4. Photochemical Generation of aza-QM·4 by Elimination of AcOH from 5

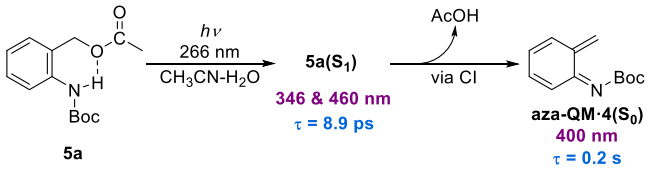

emphasize the long lifetime of this aza-QM, which allows it to react with various nucleophiles and in relatively slow Diels−Alder reactions forming cycloadducts. Consequently, photochemistry of **5** or similar molecules, may be used in organic synthesis for the construction of more complex aza-heterocycles. Moreover, it may be of interest in biological systems in the development of photocages[59] since it directly involves transformation to aza-QMs with the elimination of a potentially biologically active cargo in the form of carboxylic acid.

The inefficiency of aza-QM generation from compounds **2**−**4** can be explained by the ordering and character of the excited states. In **2** and **3**, the nitrogen is substituted with an electron-withdrawing Ac group. While this increases NH acidity, it also introduces a low-lying nπ^* state on the amide. In **2a**, this state is S_2 at the FC geometry and as shown in Figure S42 it is readily populated from the initially excited $\pi\pi^*$ state, as the barrier to the $\pi\pi^*/n\pi^*$ CI is below 0.1 eV. From the nπ^* minimum, the system reaches the S_1/S_0 CI via amide pyramidalization and C═O elongation, leaving the −OH group intact. In **3a**, the amide-localized nπ^* state (S_2) lies 0.33 eV below the −OAc-centered nπ^* state (S_4), similarly redirecting excitation to a nonreactive site. In **4a**, due to the Boc substitution, the two lowest excited states are of $\pi\pi^*$ character. However, the charge redistribution in the S_1 state leaves the dissociative C−O−H moiety largely unaffected by electronic excitation (see electron density differences in Figure S43), indicating that no significant driving force acts along the C−O coordinate. Only in **5** is excitation efficiently localized at the dissociative site, enabling efficient aza-QM generation.

CONCLUSION

Our combined experimental and computational investigation has elucidated the mechanistic details of the photochemical elimination of H_2O or AcOH from suitably substituted anilines, leading to the formation of aza-QMs.

The formation of aza-QM from **1** is a stepwise process involving OH^-elimination in the excited-state, which delivers the corresponding CIP in the S_1 state. The CIP deactivates to S_0 and dissociates to the free cation detected by ns-TA. Subsequent deprotonation yields aza-QM from **1**. In contrast, the formation of aza-QM from **5** is an ultrafast process occurring without detectable intermediates, proceeding from **5** (S_1) to the corresponding aza-QM (S_0) via internal conversion at conical intersections. For both molecules, calculations indicate the involvement of dissociative, higher-lying nσ^* states, which decrease in energy as the benzylic C−O bond elongates and cross with the initially excited $S_1(\pi\pi^*)$ state ($\pi\pi^* \rightarrow n\sigma^*$). For the model compound **5**, the calculations further suggest a possible indirect $\pi\pi^* \rightarrow n\pi^* \rightarrow n\sigma^*$ pathway involving an intermediate nπ^* state, which was detected by fluorescence and fs-TA.

The mechanistic details unveiled herein are necessary in the rational design of aza-QM precursors for their efficient generation. In particular, it was demonstrated that *N*-Boc and *O*-Ac substitutions have beneficial effects by increasing the population of the reactive conformer for elimination and introducing a localized, easily accessible nπ^* state, which provides an additional pathway for the elimination of the OAc fragment from the molecule. A thorough understanding of these mechanistic features is also crucial for the application of aza-QMs in biological contexts, where reactive intermediates may interact with biological substrates and lead to undesired effects.

COMPUTATIONAL METHODS

The conformational space of **1**−**5** in the electronic ground state was examined using the Møller−Plesset second-order (MP2) method and a range of correlation-consistent basis sets in the gas phase and in solution, where the COSMO implicit solvation model was used to approximate CH_3CN.[60,61] The photophysical properties of the most stable conformers were subsequently analyzed with the adiabatic diagrammatic construction second-order [ADC(2)] method.[62−64] Nonadiabatic dynamics simulations were performed with Tully's fewest switches surface-hopping algorithm[55] using the Zagreb surface hopping program[65] available in the Quantics suits of programs.[66,67] For detail on the computational procedure see Supporting Information Sections 4 and 5.

ASSOCIATED CONTENT

Supporting Information

The Supporting Information is available free of charge at https://pubs.acs.org/doi/10.1021/jacs.5c21621.

Contains detailed experimental procedures for the synthesis of molecules and photochemical experiments, photophysical data, UV−vis and fluorescence spectra, computational data on conformational equilibria, vertical excitations, nonadiabatic dynamics, and reaction path analyses, transient absorption spectroscopy data, coor-

https://doi.org/10.1021/jacs.5c21621
J. Am. Chem. Soc. 2026, 148, 17662−17674

dinates of the optimized structures and copies of ^{1}H and ^{13}C NMR spectra (PDF)

AUTHOR INFORMATION

Corresponding Authors

Nađa Došlić − *Department of Physical Chemistry, Ruđer Bošković Institute, 10000 Zagreb, Croatia;* orcid.org/0000-0001-6535-9020; Email: nadja.doslic@irb.hr

Jiani Ma − *Key Laboratory of Applied Surface and Colloid Chemistry of Ministry of Education, Shaanxi Provincial Key Laboratory of New Concept Sensors and Molecular Materials, School of Chemistry and Chemical Engineering, Shaanxi Normal University, Xi'an 710119, China;* orcid.org/0000-0003-3325-0762; Email: majiani@snnu.edu.cn

Nikola Basarić − *Department of Organic Chemistry and Biochemistry, Ruđer Bošković Institute, 10000 Zagreb, Croatia;* orcid.org/0000-0001-9412-9734; Email: nbasaric@irb.hr

Authors

Yifan Su − *Key Laboratory of Applied Surface and Colloid Chemistry of Ministry of Education, Shaanxi Provincial Key Laboratory of New Concept Sensors and Molecular Materials, School of Chemistry and Chemical Engineering, Shaanxi Normal University, Xi'an 710119, China*

Manuel Martinović − *Department of Physical Chemistry, Ruđer Bošković Institute, 10000 Zagreb, Croatia*

Mladena Glavaš − *Department of Organic Chemistry and Biochemistry, Ruđer Bošković Institute, 10000 Zagreb, Croatia;* Present Address: NMR Center, Ruđer Bošković Institute, Bijenička cesta 54, 10000 Zagreb, Croatia

Josip Draženović − *Department of Organic Chemistry and Biochemistry, Ruđer Bošković Institute, 10000 Zagreb, Croatia*

Complete contact information is available at: https://pubs.acs.org/10.1021/jacs.5c21621

Author Contributions

The manuscript was written through contributions of all authors. All authors have given approval to the final version of the manuscript.

Notes

The authors declare no competing financial interest.

ACKNOWLEDGMENTS

This research was funded by the National Natural Science Foundation of China (22322301) and Croatian Science Foundation (HRZZ grants no. HRZZ IP-2022-010-4658 to ND and HRZZ-IP-2019-04-8008 and HRZZ-IP-2024-05-8565 to NB). ND and NB are grateful to the ADRIS foundation for supporting this work. Dedicated to Professor Yu Fang on the occasion of his 70th birthday.

REFERENCES

(1) Rokita, S. E. *Quinone Methides*; Wiley: Hoboken, 2009.

(2) Ge, L.; Guo, Y.; Zhang, S.-L.; Phillips, D. L.; Basarić, N.; Ma, J. Mechanistic Investigations of Photochemical Generation of Quinone Methides. *Phys. Chem. Chem. Phys.* **2025**, *27*, 15272−15292.

(3) Singh, M. S.; Nagaraju, A.; Anand, N.; Chowdhury, S. ortho-Quinone Methide (o-QM): a Highly Reactive, Ephemeral and Versatile Intermediate in Organic Synthesis. *RSC Adv.* **2014**, *4*, 55924−55959.

(4) Bai, W.-J.; David, J. G.; Feng, Z.-G.; Weaver, M. G.; Wu, K.-L.; Pettus, T. R. R. The Domestication of ortho-Quinone Methides. *Acc. Chem. Res.* **2014**, *47*, 3655−3664.

(5) Uyanik, M.; Nishioka, K.; Kondo, R.; Ishihara, K. Chemoselective Oxidative Generation of ortho-Quinone Methides and Tandem Transformations. *Nat. Chem.* **2020**, *12*, 353−362.

(6) Wojciechowski, K. Aza-ortho-xylylenes in Organic Synthesis. *Eur. J. Org. Chem.* **2001**, *2001*, 3587−3605.

(7) Yang, B.; Gao, S. Recent Advances in the Application of Diels-Alder Reactions Involving o-Quinodimethanes, Aza-o-Quinone Methides and o-Quinone Methides in Natural Product Total Synthesis. *Chem. Soc. Rev.* **2018**, *47*, 7926−7953.

(8) Liao, H.-H.; Miñoza, S.; Lee, S.-C.; Rueping, M. Aza-Ortho-Quinone Methides as Reactive Intermediates: Generation and Utility in Contemporary Asymmetric Synthesis. *Chem.—Eur. J.* **2022**, *28*, No. e202201112.

(9) Steinhagen, H.; Corey, E. J. A Convenient and Versatile Route to Hydroquinolines by Inter- and Intramolecular Aza-Diels-Alder Pathways. *Angew. Chem., Int. Ed.* **1999**, *38*, 1928−1931.

(10) Lee, A.; Younai, A.; Price, C. K.; Izquierdo, J.; Mishra, R. K.; Scheidt, K. A. Enantioselective Annulations for Dihydroquinolones by in Situ Generation of Azolium Enolates. *J. Am. Chem. Soc.* **2014**, *136*, 10589−10592.

(11) Zheng, Y.-S.; Tu, L.; Gao, L.-M.; Huang, R.; Feng, T.; Sun, H.; Wang, W.-X.; Li, Z.-H.; Liu, J.-K. Accessing Benzooxadiazepines via Formal [4 + 3] Cycloadditions of Aza-o-Quinone Methides with Nitrones. *Org. Biomol. Chem.* **2018**, *16*, 2639−2642.

(12) Liu, Y.-Y.; Yu, X.-Y.; Chen, J.-R.; Qiao, M.-M.; Qi, X.; Shi, D.-Q.; Xiao, W.-J. Visible-Light-Driven Aza-ortho-quinone Methide Generation for the Synthesis of Indoles in a Multicomponent Reaction. *Angew. Chem., Int. Ed.* **2017**, *56*, 9527.

(13) Liao, H.-H.; Chatupheeraphat, A.; Hsiao, C.-C.; Atodiresei, I.; Rueping, M. Asymmetric Brønsted Acid Catalyzed Synthesis of Triarylmethanes - Construction of Communesin and Spiroindoline Scaffolds. *Angew. Chem., Int. Ed.* **2015**, *54*, 15540−15544.

(14) Walden, D. M.; Jaworski, A. A.; Johnston, R. C.; Hovey, M. T.; Baker, H. V.; Meyer, M. P.; Scheidt, K. A.; Cheong, P. H.-Y. Formation of Aza-ortho-quinone Methides under Room Temperature Conditions: Cs_2CO_3 Effect. *J. Org. Chem.* **2017**, *82*, 7183−7189.

(15) Michelin, C.; Hoffmann, N. Photosensitization and Photocatalysis Perspectives in Organic Synthesis. *ACS Catal.* **2018**, *8*, 12046−12055.

(16) Prier, C. K.; Rankic, D. A.; MacMillan, D. W. C. Visible Light Photoredox Catalysis with Transition Metal Complexes: Applications in Organic Synthesis. *Chem. Rev.* **2013**, *113*, 5322−5363.

(17) Romero, N. A.; Nicewicz, D. A. Organic Photoredox Catalysis. *Chem. Rev.* **2016**, *116*, 10075−10166.

(18) Skubi, K. L.; Blum, T. R.; Yoon, T. P. Dual Catalysis Strategies in Photochemical Synthesis. *Chem. Rev.* **2016**, *116*, 10035−10074.

(19) Kärkäs, M. D.; Porco, J. A.; Stephenson, C. R. J. Photochemical Approaches to Complex Chemotypes: Applications in Natural Product Synthesis. *Chem. Rev.* **2016**, *116*, 9683−9747.

(20) Pitre, S. P.; Overman, L. E. Strategic Use of Visible-Light Photoredox Catalysis in Natural Product Synthesis. *Chem. Rev.* **2022**, *122*, 1717−1751.

(21) Mukhina, O. A.; Cronk, W. C.; Kumar, N. N. B.; Sekhar, M. C.; Samanta, A.; Kutateladze, A. G. Intramolecular Cycloadditions of Photogenerated Azaxylylenes: An Experimental and Theoretical Study. *J. Phys. Chem. A* **2014**, *118*, 10487−10496.

(22) Mukhina, O. A.; Bhuvan Kumar, N. N.; Arisco, T. M.; Valiulin, R. A.; Metzel, G. A.; Kutateladze, A. G. Rapid Photoassisted Access to N,O,S-Polyheterocycles with Benzoazocine and Hydroquinoline Cores: Intramolecular Cycloadditions of Photogenerated Azaxylylenes. *Angew. Chem., Int. Ed.* **2011**, *50*, 9423−9428.

(23) Kumar, N. N. B.; Mukhina, O. A.; Kutateladze, A. G. Photoassisted Synthesis of Enantiopure Alkaloid Mimics Possessing

Unprecedented Polyheterocyclic Cores. *J. Am. Chem. Soc.* **2013**, *135*, 9608−9611.
(24) Mukhina, O. A.; Kuznetsov, D. M.; Cowger, T. M.; Kutateladze, A. G. Amino Azaxylylenes Photogenerated from o-Amido Imines: Photoassisted Access to Complex Spiro-Poly-Heterocycles. *Angew. Chem., Int. Ed.* **2015**, *54*, 11516−11520.
(25) Kuznetsov, D. M.; Mukhina, O. A.; Kutateladze, A. G. Photoassisted Synthesis of Complex Molecular Architectures: Dearomatization of Benzenoid Arenes with Aza-o-xylylenes via an Unprecedented [2 + 4] Reaction Topology. *Angew. Chem., Int. Ed.* **2016**, *55*, 6988−6991.
(26) Kuznetsov, D. M.; Kutateladze, A. G. Step-Economical Photoassisted Diversity-Oriented Synthesis: Sustaining Cascade Photoreactions in Oxalyl Anilides to Access Complex Polyheterocyclic Molecular Architectures. *J. Am. Chem. Soc.* **2017**, *139*, 16584−16590.
(27) Yang, C.; Wan, P. Photosolvolysis of 2-Aminobenzyl Alcohol in Aqueous Solution. *J. Photochem. Photobiol., A* **1994**, *80*, 227−232.
(28) Wu, T.-H.; Su, Z.-S.; Sung, R.; Sung, K. Aza-ortho-Quinone Methide and Its Conjugated Acid: Reactivity, Stability and Acidity. *ChemPhysChem* **2020**, *21*, 307−312.
(29) Wang, M.; Li, S.; Wang, J.; Zhang, O.; Du, H.; Jiang, D.; Wu, Z.; Deng, Y.; Kang, Y.; Pan, P.; Li, D.; Wang, X.; Yao, X.; Hou, T.; Hsieh, C.-Y. ClickGen: Directed Exploration of Synthesizable Chemical Space via Modular Reactions and Reinforcement Learning. *Nat. Commun.* **2024**, *15*, 10127.
(30) Chow, S. Y.; Nelson, A. Embarking on a Chemical Space Odyssey. *J. Med. Chem.* **2017**, *60*, 3591−3593.
(31) Rydholm, E.; Bastys, T.; Svensson, E.; Kannas, C.; Engkvist, O.; Kogej, T. Expanding the Chemical Space Using a Chemical Reaction Knowledge Graph. *Digital Discovery* **2024**, *3*, 1378−1388.
(32) MacDonell, R. J.; Schuurman, M. S. Site-Selective Isomerization of Cyano-Substituted Butadienes: Chemical Control of Nonadiabatic Dynamics. *J. Phys. Chem. A* **2019**, *123*, 4693−4701.
(33) MacDonell, R. J.; Corrales, M. E.; Boguslavskiy, A. E.; Bañares, L.; Stolow, A.; Schuurman, M. S. Substituent Effects on Nonadiabatic Excited State Dynamics: Inertial, Steric, and Electronic Effects in Methylated Butadienes. *J. Chem. Phys.* **2020**, *152*, 084308.
(34) Zimmerman, H. E. The Meta Effect in Organic Photochemistry: Mechanistic and Exploratory Organic Photochemistry. *J. Am. Chem. Soc.* **1995**, *117*, 8988−8991.
(35) Chakraborty, P.; Couto, R. C.; List, N. H. Deciphering Methylation Effects on $S_2(\pi\pi^*)$ Internal Conversion in the Simplest Linear α,β-Unsaturated Carbonyl. *J. Phys. Chem. A* **2023**, *127*, 5360−5373.
(36) Mirón, G. D.; Semelak, J. A.; Grisanti, L.; Rodriguez, A.; Conti, I.; Stella, M.; Velusamy, J.; Seriani, N.; Došlić, N.; Rivalta, I.; Garavelli, M.; Estrin, D. A.; Kaminski Schierle, G. S.; González Lebrero, M. C.; Hassanali, A.; Morzan, U. N. The Carbonyl-Lock Mechanism Underlying Non-Aromatic Fluorescence in Biological Matter. *Nat. Commun.* **2023**, *14*, 7325.
(37) Whitesell, J. K.; Minton, M. A.; Tran, V. D. The NEER Principle. Ground-State Conformational Bias in Triene Photocyclizations. *J. Am. Chem. Soc.* **1989**, *111*, 1473−1476.
(38) Mazzucato, U.; Momicchioli, F. Rotational Isomerism in trans-1,2-Diarylethylenes. *Chem. Rev.* **1991**, *91*, 1679−1719.
(39) Satzger, H.; Townsend, D.; Zgierski, M. Z.; Patchkovskii, S.; Ullrich, S.; Stolow, A. Primary Processes Underlying the Photostability of Isolated DNA Bases: Adenine. *Proc. Natl. Acad. Sci. U.S.A.* **2006**, *103*, 10196−10201.
(40) Bhattacherjee, A.; Pemmaraju, C. D.; Schnorr, K.; Attar, A. R.; Leone, S. R. Ultrafast Intersystem Crossing in Acetylacetone via Femtosecond X-ray Transient Absorption at the Carbon K-Edge. *J. Am. Chem. Soc.* **2017**, *139*, 16576−16583.
(41) Sapunar, M.; Ayari, T.; Došlić, N. Comparative Study of the Photodynamics of Malonaldehyde and Acetylacetone. *Chem. Phys.* **2018**, *515*, 622−627.
(42) Haugen, E. A.; Hait, D.; Scutelnic, V.; Xue, T.; Head-Gordon, M.; Leone, S. R. Ultrafast X-ray Spectroscopy of Intersystem Crossing in Hexafluoroacetylacetone: Chromophore Photophysics and Spectral Changes in the Face of Electron-Withdrawing Group. *J. Phys. Chem. A* **2023**, *127*, 634−644.
(43) Chakraborty, P.; Couto, R. C.; List, N. H. Electronic and Inertial Effects of Methylation on Excited-State Hydrogen Transfer. *J. Phys. Chem. A* **2026**, *130*, 1090−1103.
(44) Sobolewski, A. L.; Domcke, W. Conical Intersections Induced by Repulsive $^1\pi\sigma^*$ States in Planar Organic Molecules: Malonaldehyde, Pyrrole and Chlorobenzene as Photochemical Model Systems. *Chem. Phys.* **2000**, *259*, 181−191.
(45) Conical Intersections, Theory, Computation and Experiment. *Advanced Series in Physical Chemistry*; Domcke, W., Yarkony, D. R., Köppel, H., Eds.; World Scientific Publishing co., 2011; Vol. *17*
(46) Matsika, S.; Krause, P. Nonadiabatic Events and Conical Intersections. *Annu. Rev. Phys. Chem.* **2011**, *62*, 621−643.
(47) Rahn, R. O. Potassium Iodide as a Chemical Actinometer for 254 nm Radiation: Use of Iodate as an Electron Scavenger. *Photochem. Photobiol.* **1997**, *66*, 450−455.
(48) Goldstein, S.; Rabani, J. The Ferrioxalate and Iodide-Iodate Actinometers in the UV Region. *J. Photochem. Photobiol.* **2008**, *193*, 50−55.
(49) Veljković, J.; Uzelac, L.; Molčanov, K.; Mlinarić-Majerski, K.; Kralj, M.; Wan, P.; Basarić, N. Sterically Congested Adamantylnaphthalene Quinone Methides. *J. Org. Chem.* **2012**, *77*, 4596−4610.
(50) Škalamera, Đ.; Bohne, C.; Landgraf, S.; Basarić, N. Photodeamination Reaction Mechanism in Aminomethyl p-Cresol Derivatives: Different Reactivity of Amines and Ammonium Salts. *J. Org. Chem.* **2015**, *80*, 10817−10828.
(51) Arumugam, S.; Popik, V. V. Photochemical Generation and the Reactivity of o-Naphthoquinone Methides in Aqueous Solutions. *J. Am. Chem. Soc.* **2009**, *131*, 11892−11899.
(52) Boens, N.; Qin, W.; Basarić, N.; Hofkens, J.; Ameloot, M.; Pouget, J.; Lefèvre, J. P.; Valeur, B.; Gratton, E.; VandeVen, M.; Silva, N. D.; Engelborghs, Y.; Willaert, K.; Sillen, A.; Rumbles, G.; Phillips, D.; Visser, A. J. W. G.; Van Hoek, A.; Lakowicz, J. R.; Malak, H.; Gryczynski, I.; Szabo, A. G.; Krajcarski, D. T.; Tamai, N.; Miura, A. Fluorescence Lifetime Standards for Time and Frequency Domain Fluorescence Spectroscopy. *Anal. Chem.* **2007**, *79*, 2137−2149.
(53) Sobolewski, A. L.; Domcke, W.; Dedonder-Lardeux, C.; Jouvet, C. Excited-State Hydrogen Detachment and Hydrogen Transfer Driven by Repulsive $\pi\sigma^*$ States: A New Paradigm for Nonradiative Decay in Aromatic Biomolecules. *Phys. Chem. Chem. Phys.* **2002**, *4*, 1093−1100.
(54) Ashfold, M. N. R.; Cronin, B.; Devine, A. L.; Dixon, R. N.; Nix, M. G. D. The Role of $\pi\sigma^*$ Excited States in the Photodissociation of Heteroaromatic Molecules. *Science* **2006**, *312* (5780), 1637−1640.
(55) Tully, J. C. Molecular Dynamics with Electronic Transitions. *J. Chem. Phys.* **1990**, *93*, 1061−1071.
(56) McClelland, R. A.; Kanagasabapathy, V. M.; Banait, N. S.; Steenken, S. Reactivities of Triarylmethyl and Diarylmethyl Cations with Azide Ion Investigated by Laser Flash Photolysis. Diffusion-Controlled Reactions. *J. Am. Chem. Soc.* **1991**, *113*, 1009−1014.
(57) Osuna, S.; Swart, M.; Baerends, E. J.; Bickelhaupt, F. M.; Sola, M. Homolytic versus Heterolytic Dissociation of Alkalimetal Halides: The Effect of Microsolvation. *ChemPhysChem* **2009**, *10*, 2955−2965.
(58) Wang, Q.; Agarawal, V.; Hermes, M. R.; Motta, M.; Rice, J. E.; Jones, G. O.; Gagliardi, L. Distinguishing homolytic vs heterolytic bond dissociation of phenylsulfonium cations with localized active space methods. *J. Chem. Phys.* **2024**, *161*, 014106.
(59) Ellis-Davies, G. C. R. Reverse Engineering Caged Compounds: Design Principles for their Application in Biology. *Angew. Chem. Int. Ed.* **2023**, *62*, No. e202206083.
(60) Klamt, A. Conductor-like Screening Model for Real Solvents: A New Approach to the Quantitative Calculation of Solvation Phenomena. *J. Phys. Chem.* **1995**, *99*, 2224−2235.
(61) Klamt, A.; Jonas, V.; Bürger, T.; Lohrenz, J. C. W. Refinement and Parametrization of COSMO-RS. *J. Phys. Chem. A* **1998**, *102*, 5074−5085.

(62) Schirmer, J. Beyond the Random-Phase Approximation: A New Approximation Scheme for the Polarization Propagator. *Phys. Rev. A:At., Mol., Opt. Phys.* **1982**, *26*, 2395−2416.
(63) Trofimov, A. B.; Schirmer, J. An Efficient Polarization Propagator Approach to Valence Electron Excitation Spectra. *J. Phys. B:At., Mol. Opt. Phys.* **1995**, *28*, 2299−2324.
(64) Dreuw, A.; Wormit, M. The Algebraic Diagrammatic Construction Scheme for the Polarization Propagator for the Calculation of Excited States. *Wiley Interdiscip. Rev. Comput. Mol. Sci.* **2015**, *5*, 82−95.
(65) Sapunar, M.; Piteša, T.; Davidović, D.; Došlić, N. Highly Efficient Algorithms for CIS Type Excited State Wave Function Overlaps. *J. Chem. Theory Comput.* **2019**, *15*, 3461−3469.
(66) Coonjobeeharry, J.; Spinlove, K. E.; Sanz Sanz, C.; Sapunar, M.; Došlić, N.; Worth, G. A. Mixed-Quantum-Classical or Fully-Quantized Dynamics? A Unified Code to Compare Methods. *Philos. Trans. R. Soc., A* **2022**, *380*, 20200386.
(67) Worth, G. Quantics [Computer software], GitLab, 2025. https://gitlab.com/quantics/quantics (accessed April 07, 2026).

https://doi.org/10.1021/jacs.5c21621
J. Am. Chem. Soc. 2026, 148, 17662−17674